SPECIAL MATERHORN COLLECTION

Reasons for the Extremely High-Ranging Planetary Boundary Layer over the Western Tibetan Plateau in Winter

XUELONG CHEN,* BOJAN ŠKERLAK,+ MATHIAS W. ROTACH,# JUAN A. AÑEL,@,& ZHONBGO SU,* YAOMING MA,**,++ AND MAOSHAN LI##,*

* *Faculty of Geo-Information Science and Earth Observation, University of Twente, Enschede, Netherlands*
+ *Institute for Atmospheric and Climate Science, ETH Zurich, Zurich, Switzerland*
# *Institute of Atmospheric and Cryospheric Sciences, University of Innsbruck, Innsbruck, Austria*
@ *Smith School of Enterprise and the Environment, University of Oxford, Oxford, United Kingdom*
& *Environmental Physics Laboratory, Science Faculty, Vigo University, Ourense, Spain*
** *Key Laboratory of Tibetan Environment Changes and Land Surface Processes, Institute of Tibetan Plateau Research, Chinese Academy of Sciences, Beijing, China*
++ *CAS Center for Excellence in Tibetan Plateau Earth Sciences, Beijing, China*
Key Laboratory of Land Surface Process and Climate Change in Cold and Arid Regions, Cold and Arid Regions Environmental and Engineering Research Institute, Chinese Academy of Sciences, Lanzhou, China

(Manuscript received 2 June 2015, in final form 3 March 2016)

ABSTRACT

The planetary boundary layer (PBL) over the Tibetan Plateau (with a mean elevation about 4 km above sea level) reaches an unmatched height of 9515 m above sea level. The proximity of this height to the tropopause facilitates an exchange between the stratosphere and the boundary layer. However, the underlying mechanisms responsible for this unique PBL have remained uncertain. Here, the authors explore these mechanisms and their relative importance using measurements of the PBL, the associated surface fluxes, and single-column and regional numerical simulations, as well as global reanalysis data. Results indicate that the dry conditions of both ground soil and atmosphere in late winter cannot explain the special PBL alone. Rather, the results from a single-column model demonstrate the key influence of the stability of the free atmosphere upon the growth of extremely deep PBLs over the Tibetan Plateau. Simulations with the numerical weather prediction model Consortium for Small-Scale Modelling (COSMO) exhibit good correspondence with the observed mean PBL structure and realistic turbulent kinetic energy distributions throughout the PBL. Using ERA-Interim, the authors furthermore find that weak atmospheric stability and the resultant deep PBLs are associated with higher upper-level potential vorticity (PV) values, which in turn correspond to a more southerly jet position and higher wind speeds. Upper-level PV structures and jet position thus influence the PBL development over the Tibetan Plateau.

1. Introduction

The planetary boundary layer (PBL) is the lowest layer of the atmosphere and is in contact with the surface of Earth. It determines the exchange of heat, momentum, moisture, and chemical constituents between the surface and the free atmosphere (Yanai and Li 1994; Baklanov et al. 2011). The PBL over the Tibetan Plateau (TP), one of the largest and the highest plateau on Earth (mean elevation about 4 km MSL), can even influence weather systems and climate on regional to global scales (e.g., Li and Gao 2007; Tao and Ding 1981). Correct representation of the plateau PBL in numerical weather prediction (NWP) models is thus vital for understanding the thermal and dynamic effects of the TP on Asian weather and climate, especially when studying the role of the TP in the Asian monsoon system (Xu et al. 2002; Yang et al. 2004; Boos and Kuang 2010; Wu et al. 2012). A clear understanding of processes involved in PBL dynamics over the TP is therefore crucial.

In the past two decades, several comprehensive field experiments have been conducted to analyze the land surface processes and the structure of the PBL over the

Corresponding author address: Xuelong Chen, Faculty of Geo-Information Science and Earth Observation, University of Twente, Hengelostraat 99, Enschede 7500AE, Netherlands.
E-mail: x.chen@utwente.nl

DOI: 10.1175/JAS-D-15-0148.1

TP (Yanai et al. 1992; Yanai and Li 1994; Xu et al. 2002; Yang et al. 2004; Li et al. 2006; Sun et al. 2007). Several studies have reported the presence of a pronounced mixed layer (ML) prior to the onset of the monsoon (e.g., Luo and Yanai 1984). Recently, it was found that the top of the PBL over the plateau can reach as high as 9515 m above mean sea level (MSL, corresponding to approximately 5 km above ground level) in February (Chen et al. 2013)—higher than any previously reported PBL worldwide (see also Table 1). Although very large PBL depths of more than 5 km have been reported in desert and arid regions (see Table 1), the elevation of the surface in these regions is typically not more than 1 km MSL. Moreover, the depth of the PBL over the TP actually is typically greater than it is over the surrounding lowlands (Yang et al. 2004; Zuo et al. 2005; Li et al. 2006; Fan et al. 2011). This unique combination of very-high-PBL depth and very high orography leads to an extremely high-ranging PBL top, at times reaching the neighborhood of the tropopause. This facilitates the exchange of chemical constituents between the PBL and the stratosphere with important impacts on atmospheric chemistry [see Škerlak et al. (2014) and references therein].

In general, the development of the PBL depth is determined by the heating at the surface [i.e., the sensible heat fluxes (Zhang et al. 2011; Yang et al. 2004)] on the one hand and the stratification of the overlying layer into which the PBL grows (Freire and Dias 2013; Blay-Carreras et al. 2014) on the other hand. The former is influenced by evaporation processes competing for the available energy and thus the soil moisture conditions (Eltahir 1998; Zhang et al. 2011; Sanchez-Mejia and Papuga 2014), snow cover (Ueno et al. 2012), and local terrain (Whiteman 1990; Nyeki et al. 2000; Whiteman et al. 2000; Rotach and Zardi 2007; Yang et al. 2004; Seidel et al. 2012). It has been argued that land surface heterogeneity (Ao et al. 2012; Seidel et al. 2012; Yanai et al. 1992; Yanai and Li 1994) can enhance the near-surface mixing and hence the growth of the PBL. The development of an elevated PBL (such as over the TP) may further be influenced by low air density, relatively cold temperatures, and a modified radiation balance (Yang et al. 2004).

Many regional studies in both hemispheres determined seasonal variations in PBL depths using radiosonde data. For example, Holzworth (1967) noted that the highest PBL in New York occurs between April and August (boreal summer), whereas the lowest PBL occurs during boreal winter. In southern Africa, the PBL top is highest in September and October, whereas it is the lowest between May and August (Korhonen et al. 2014). Cuesta et al. (2008) found that the largest PBL

TABLE 1. Radiosonde-retrieved high PBLs worldwide.

Reference	Station location	Season	Site elevation (km MSL)	PBL depth (km)	Elevation of PBL top (km MSL)	Note
Li et al. (2006)	Qomolangma, Tibetan Plateau (28.14°N, 86.85°E)	May	4.7	3.8	8.5	Monsoon onset
Zuo et al. (2005)	Anduo, Tibetan Plateau (30.54°N, 100.69°E)	June	4.7	3.5	8.2	Monsoon onset
Zhang et al. (2003)	Damxung, Tibetan Plateau (30.47°N, 91.10°E)	June	4.2	2.3	6.5	Near monsoon period
Yang et al. (2004)	Naqu, Tibetan Plateau (32.24°N, 91.64°E)	June	4.7	3.0	7.7	Monsoon onset
Chen et al. (2013)	Gerze, Tibetan Plateau (32.17°N, 84.03°E)	February	4.4	5.0	9.4	Winter
Gamo (1996)	Africa, Asia—desert	July	1.1	4.0–6.0	5.1–7.1	Summer
Cuesta et al. (2008)	Sahara Desert (22.79°N, 5.53°E)	June	1.1	6.0	7.1	Summer
Han et al. (2012)	Badanjilin Desert (39.28°N, 102.22°E)	August	1.4	3.0	5.1	Summer
Zhang et al. (2011)	Gobi Desert (40.17°N, 94.52°E)	July	1.1	4.0	5.1	Summer
Takemi (1999)	Semiarid area in Yinchuan (38.49°N, 106.24°E)	May	1.1	4.0	5.1	Spring
Raman et al. (1990)	New Delhi (28.43°N, 77.18°E)	June	0.2	4.7	4.9	Premonsoon
Whiteman et al. (2000)	Mexican Plateau basin (several stations)	February–March	2.3	3.0	5.3	Winter/dry season
Nyeki et al. (2000)	European Alps (46.55°N, 77.98°E)	July	1.0–3.6	0.6–3.2	4.2	Summer

depth occurs during summer over the Sahara Desert and Chan and Wood (2013) reported that the PBL depth over extratropical land regions peaks during summer. A significant seasonal difference in the PBL depth has been reported in some regions, including the United States and Europe (Seidel et al. 2012), Algeria (Cuesta et al. 2008), and the Loess Plateau in China (Zhang et al. 2012). A recent global PBL climatology based on ERA-Interim data showed that the deepest PBLs in both hemispheres typically occur in the respective summer seasons [von Engeln and Teixeira (2013), their Fig. 5]. For the TP, however, the ERA-Interim data exhibit the largest PBL depths around March in correspondence to the radio sounding observations.

On the other hand, the mean PBL depth over the TP based on spaceborne remote sensing observations (von Engeln et al. 2005; McGrath-Spangler and Denning 2013) appears to be largest in summer [see Figs. 3 and 5 in McGrath-Spangler and Denning (2013)]. These remote sensing observations have a quite low horizontal resolution (a few hundred kilometers). Hence, the PBL depths derived from spaceborne remote sensing represent an average over larger horizontal areas, which might at least partly explain the discrepancy to the results based on reanalysis data.

The goal of this study is to understand why the PBL on the TP reaches such high altitudes and to understand its seasonal cycle. To this end, we combine in situ measurements on the TP during three different seasons in 2008 (radiosondes and land surface conditions) with models of varying complexity to identify key parameters driving the PBL growth over the TP. Using reanalysis data, we put these findings in a climatological context, determine synoptic-scale conditions leading to high PBLs, and statistically quantify the dependence of PBL depth on these key variables.

This paper is organized as follows: in section 2, we present radiosonde and ground-based measurement techniques (section 2a), an idealized single-column model for boundary layer growth (section 2b), the regional NWP model setup (section 2c), and the ERA-Interim dataset (section 2d). In section 3, we then present the results of three intensive observation periods (IOPs) on the TP (sections 3a and 3b), the slab model sensitivity study (section 3c), and regional NWP analysis (section 3d). In section 3e, the results of the climatological and statistical investigation are presented. Finally, we discuss and summarize our study in section 4.

2. Data and methods

The PBL depth is a crucial parameter that is used to describe diurnal, synoptic, and climatological processes, connections between the surface and the free troposphere, and air pollution dilution (Stull 1988; Seibert et al. 2000; Ao et al. 2012). The convective PBL top is generally defined by sharp gradients in one or more of the following variables: humidity, temperature, turbulence, wind, tracers (including aerosol particles), or boundary layer cloud droplets (Stull 1988; Seidel et al. 2010).

These gradients are detectable using measurements from radio soundings (Rs) or surface-based and spaceborne remote sensors such as lidar (McGrath-Spangler and Denning 2013) or radio occultation (Chan and Wood 2013; Kursinski et al. 1997; Ao et al. 2012). Rs measurements constitute the most widely applied operational method but the PBL depth can also be determined from model output and (re)analysis data.

a. Radiosonde and ground-based measurements

During three IOPs, four Vaisala RS-92 radiosondes were released every day, at 0100, 0700, 1300, and 1900 local time (LT) (LT corresponds to the Beijing standard time, UTC+8), from Gerze station on the TP (32.17°N, 84.03°E, 4415 m MSL). Gerze station is suitable for studying the PBL over the Tibetan Plateau because there are no high mountains nearby. Therefore, it is not necessary to account for topographic effects in the analysis. IOP1 lasted from 25 February to 19 March 2008, IOP2 from 13 May to 12 June 2008, and IOP3 from 7 to 16 July 2008. Thus, three different seasons were covered. The Rs data have a vertical resolution of approximately 10 m. Near-surface wind speed, wind direction, temperature, and relative humidity measurements were obtained at 0.5 and 10 m above ground, whereas pressure, precipitation, and the four radiation components—that is, downward shortwave radiation (DSR), upward shortwave radiation (USR), downward longwave radiation (DLR), and upward longwave radiation (ULR)—were measured at a height of 1.5 m. Turbulent, sensible, and latent heat fluxes were estimated via the bulk transfer method using the meteorological measurements collected at heights of 0.5 and 10 m (Chen et al. 2013) and nondimensional profiles following Högström (1996). The roughness length was calculated with a method previously described by Yang et al. (2003).

Here we determined the Rs PBL depth using the parcel method, which is known to yield reliable results (Holzworth 1964; Seibert et al. 2000; Hennemuth and Lammert 2006). The parcel method defines the PBL depth according to the height at which the actual potential temperature profile intersects the dry-adiabatic profile starting from the temperature measured near ground level. As an alternative method, the bulk Richardson number (Ri_B) is also used to determine the

PBL depth to validate the parcel method results. This number is defined as follows (Vogelezang and Holtslag 1996; Stull 1988):

$$\mathrm{Ri}_B = \frac{gz[\Theta(z) - \Theta(s)]}{\Theta(s)[u(z)^2 + v(z)^2]}, \tag{1}$$

where $\Theta(z)$ and $\Theta(s)$ are the potential temperatures at reference height z and surface s; $u(z)$ and $v(z)$ are the zonal and meridional velocity components, respectively; and g is the acceleration due to gravity—that is, 9.8 m s^{-2}. We computed Ri_B based on surface information from the lowest level of the sounding data.

The bulk Richardson number PBL depth, following Troen and Mahrt (1986), is defined as the height at which Ri_B reaches a critical value (≈0.25) (Seidel et al. 2012; Xie et al. 2003). Generally, a Ri_B smaller than this critical value is considered to be a condition for turbulence associated with the dynamical instability of the atmosphere (Nath et al. 2010). In such conditions, turbulence can develop because shear dominates over the damping influence of the temperature inversion. For Ri_B exceeding 0.25, the temperature inversion is dominant and turbulent fluctuations are suppressed. If Ri_B is negative, the region is convectively unstable (Hecht et al. 2004).

As the parcel and Ri_B methods exhibit highly consistent results for the Gerze station [see also Chen (2013)], we only show the results from the parcel method in this study.

b. Single-column model for boundary layer growth

One of the most widely used analytical slab models for the growth of the convective boundary layer was developed by Batchvarova and Gryning (1991, hereafter BG91). This highly idealized slab model is based on a simplified turbulent kinetic energy (TKE) equation and accounts for the temperature difference across the top of the mixed layer by assuming an infinitesimally shallow entrainment layer and specifying the stability of the overlying free troposphere γ.

The model accounts for the effects of convective and mechanical turbulence and has been used to study the growth of fully convective or near-neutral mixed layers. It requires an initial value for the boundary layer height h that may be estimated as the (nocturnal) boundary layer height immediately before the surface sensible heat flux first becomes positive. The surface sensible heat flux ($\overline{w'\Theta'_0}$), friction velocity ($U_\star$), Obukhov length (L), and γ must be known from the initialization time to the time when the ML top is to be determined (as a result of missing data, γ is often assumed to be constant). The latter is then calculated by integrating the equation for the ML growth rate:

$$\frac{dh}{dt} = \frac{\overline{w'\Theta'_0}}{\gamma}\left\{\frac{h^2}{(1-2A)h - 2B\kappa L} + \frac{CU_\star^2 T}{\gamma g[(1+A)h - B\kappa L]}\right\}^{-1}, \tag{2}$$

where $\kappa = 0.4$ is the von Kármán constant and $A = 0.2$, $B = 2.5$, and $C = 8$ are model parameters. These enter the model through an energy budget equation for the mixed layer in order to estimate the heat flux from above the boundary layer through entrainment. The chosen parameter values are those recommended by BG91 based on various experimental and theoretical studies from the literature.

c. Numerical weather prediction model COSMO

Consortium for Small-Scale Modelling (COSMO) is a limited-area, nonhydrostatic NWP model that is operationally used by many national weather services in Europe (Baldauf et al. 2011). We use model version 4.24 with a rotated pole to maximize the regularity of the coordinate grid. The area around the Tibetan Plateau is centered around 0° longitude and latitude in the rotated coordinates. The horizontal grid spacing is set to 0.0625° (approximately 7 km) and 79 hybrid vertical levels are used (with a grid spacing of approximately 10 m near the ground and 100 m near the tropopause). The simulation domain extends from −20° to 20° rotated longitude and −15° to 15° rotated latitude (641 × 481 grid points), which corresponds to approximately 60° to 120°E and from 15° to 50°N (see Fig. 6 below) and reaches well into the stratosphere. Land use data are obtained from the default dataset of the German National Weather Service. The model time step is set to 40 s and model output is written to disk every hour.

We cover the three IOPs with overlapping 7-day simulations to reduce forecast errors due to long model run times. COSMO is initialized using global operational analyses from the European Centre for Medium-Range Weather Forecasts (ECMWF), which are interpolated onto a 1° × 1° horizontal grid and 91 vertical levels. These analyses are also used to update the boundaries every 6 h. The PBL depth is diagnosed from the COSMO simulations using the bulk Richardson number method with a default critical value of $\mathrm{Ri}_B = 0.22$ in unstable conditions (Vogelezang and Holtslag 1996) and $\mathrm{Ri}_B = 0.33$ in stable conditions (Wetzel 1982). The regime is determined using the virtual potential temperature lapse rate near the ground. Model-diagnosed PBL depth is then extracted at the grid point closest to Gerze station. Clearly, the diagnosed PBL heights exhibit some sensitivity to the chosen threshold values (0.22 and 0.33, respectively). Still, they have been optimized by the given references and show among the smallest rms differences to

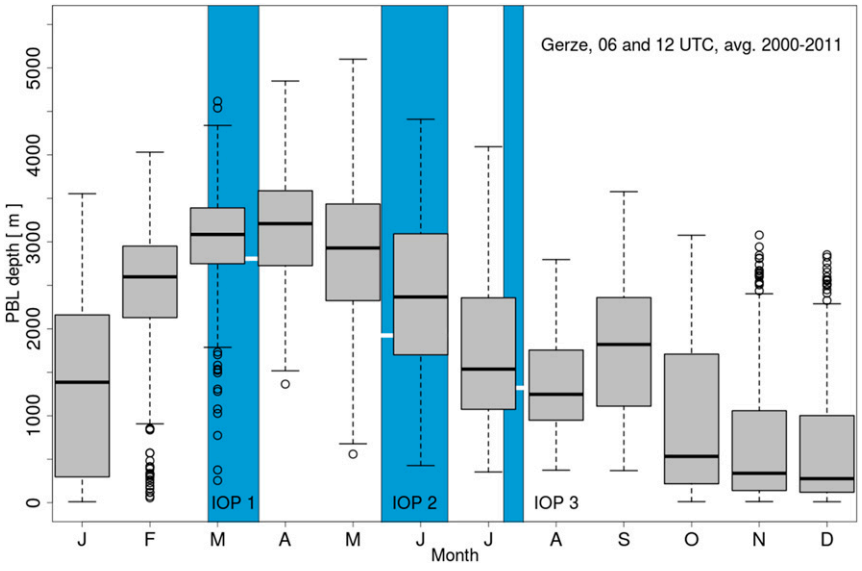

FIG. 1. Box-and-whisker plot of PBL depth (m AGL) at 0600 UTC (1400 LT) and 1200 UTC (2000 LT) based on ERA-Interim data. The values at the grid point closest to Gerze station (GER) have been extracted for the period 2000–11 and grouped by month. The black line is the median, 50% of the data lie in the gray box [between 25th and 75th percentiles, the so-called interquartile range (IQR)], and the whiskers are placed at a distance of 1.5 times the IQR away from the box. Data points outside the whiskers are marked as outliers (circles). Areas shaded in blue indicate IOP1, IOP2, and IOP3, respectively, and the white horizontal lines show the median of all soundings at 1300 and 1900 LT in each IOP.

observations in complex terrain when compared to other methods (Szintai et al. 2009).

d. *ERA-Interim data*

ERA-Interim is a state-of-the-art reanalysis dataset from ECMWF. It is available at T255L60 resolution at 0000, 0600, 1200, and 1800 UTC from 1 January 1979 to present day (Simmons et al. 2007; Dee et al. 2011). In this study, we use the 12 yr from 2000 to 2011. Primary analysis fields (e.g., wind and temperature) are horizontally interpolated on a regular longitude–latitude grid with 1° resolution. Secondary fields such as potential vorticity (PV) and potential temperature are then calculated on the 60 original hybrid model levels (reaching from the surface to 0.1 hPa). PBL depth in ERA-Interim is also diagnosed using the bulk Richardson number method with a critical value of $\mathrm{Ri}_B = 0.25$ as often employed in the literature (e.g., McGrath-Spangler and Molod 2014; Seidel et al. 2012). A sensitivity study with $\mathrm{Ri}_B = 0.5$ yielded only minor differences in the diagnosed PBL heights for most of the days (with the exception of two days in IOP2 and one day in IOP3; not shown).

3. Results

In this section, we first present the seasonal cycle of PBL depth over Gerze station derived from ERA-Interim data and compare it to the radiosonde data (section 3a). Then we explore the relationship between PBL depth obtained from radiosonde data and in situ surface measurements (section 3b). The idealized BG91 model is used in section 3c to investigate the relative importance of processes influencing PBL growth. This one-dimensional analysis is complemented by the fully three-dimensional NWP model COSMO in section 3d. As we find good agreement between measured data, COSMO simulations, and ERA-Interim data, we use the latter to compile composites of the meteorological situation during days with very high and very low PBLs and perform statistical analysis of influencing parameters in section 3e.

a. *Seasonal cycle and radiosondes*

We extracted the PBL depth from the ERA-Interim dataset at the grid point nearest to Gerze station at 0600 and 1200 UTC every day between January 2000 and December 2011. A box-and-whisker plot of the resulting seasonal cycle, with the IOPs marked as blue areas, is shown in Fig. 1.

The PBL depth derived from the soundings during the three intensive observation periods (IOP1, IOP2, and IOP3; cf. section 2a) are shown in Fig. 2 (green dashed line and triangles). PBL depths in the afternoon during IOP1 regularly reach 4 km and more (9 out of 24

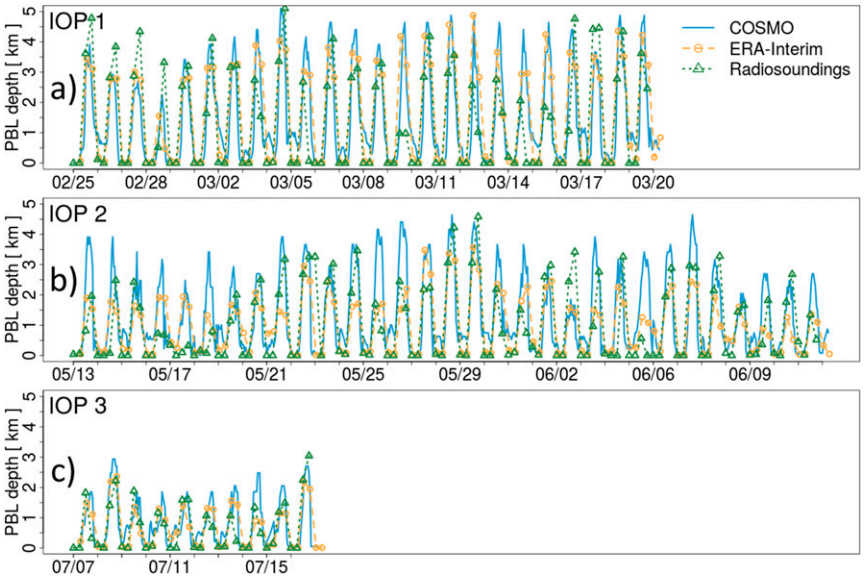

FIG. 2. PBL depth time series at Gerze station during (a) IOP1, (b) IOP2, and (c) IOP3 in 2008 as calculated from COSMO output (blue line), ERA-Interim (orange dashed line, circles, data at 0000, 0600, 1200, and 1800 UTC), and radiosonde data (green dashed line, triangles, data at 0500, 1100, 1700, and 2300 UTC). Tick marks every 24 h and dates are labeled as month/day.

soundings at 1900), whereas during IOP2, only two radio soundings (out of 31) exhibit a PBL depth exceeding 4 km at the same time of the day. Most other PBL depths (22 out of 31) in the afternoon during IOP2 are not greater than 3 km. The PBL depths measured during IOP3 rarely exceed 2 km (only in 2 out of 10 cases at 1900). The median PBL depth at 1300 and 1900 during IOP1, -2, and -3 is 2830, 2010, and 1260 m, respectively (white horizontal lines in Fig. 1). Therefore, based on the Rs observations, deep PBLs are commonly found in winter over the TP and are rare during summer, confirming ERA-Interim. The discrepancy between ERA-Interim and radiosonde PBL depth could be explained by using a variable Ri_B value. This pattern is distinctly different from the situation that occurs over most land areas, where high PBLs usually occur in summer and low PBLs are present in winter (von Engeln and Teixeira 2013) (see also section 1).

b. *Surface measurements*

Since the height of the PBL is often related to the available heat energy at the surface and hence the corresponding variables describing the energy balance at the surface (e.g., Eltahir 1998; Yang et al. 2004; Endo et al. 2008; Zhang et al. 2011; Sanchez-Mejia and Papuga 2014) we first assess to what degree such relations can be found during the three IOPs at the Gerze site on the TP. Table 2 summarizes the determination coefficients (R^2) from linear regression analysis between the observed growth rate ($\Delta h/\Delta t$) of the PBL and the following surface variables: downward shortwave radiation, sensible heat flux (H), latent heat flux (LE), friction velocity ($U_\star$), land surface temperature (LST), soil moisture (SM), surface air temperature (T_{air}), and relative humidity (RH). Scatterplots between $\Delta h/\Delta t$ for the three IOPs and the first four of these variables are shown in Fig. 3.

It is first of all noted that generally the relation between the PBL growth rate and the surface variables is very weak (Table 2). Only the dominant input to available radiative energy during daytime (DSR) and consequently the surface sensible heat flux exhibit R^2 values that are substantially different from zero in all three IOPs. Latent heat flux is different between the three seasons (IOPs) but there is no sensitive dependence on

TABLE 2. Coefficient of determination R^2 from linear regression of PBL growth rate and ground surface energy variables. DSR: downward shortwave radiation; H: sensible heat flux; LE: latent heat flux; $U_\star$: friction velocity; LST: land surface temperature; SM: surface soil moisture; T_{air}: surface air temperature; RH: relative humidity. IOP1/-2/-3 refer to the IOPs as defined in section 1 with variable length. Two soundings per day (1300 and 1900 LT) are used in the analysis.

	DSR	H	LE	$U_\star$	LST	SM	LST − T_{air}	RH
IOP1	0.13	0.16	0.03	0.20	0.00	0.01	0.04	0.16
IOP2	0.36	0.29	0.04	0.00	0.41	0.08	0.26	0.58
IOP3	0.49	0.17	0.06	0.17	0.10	0.01	0.11	0.20

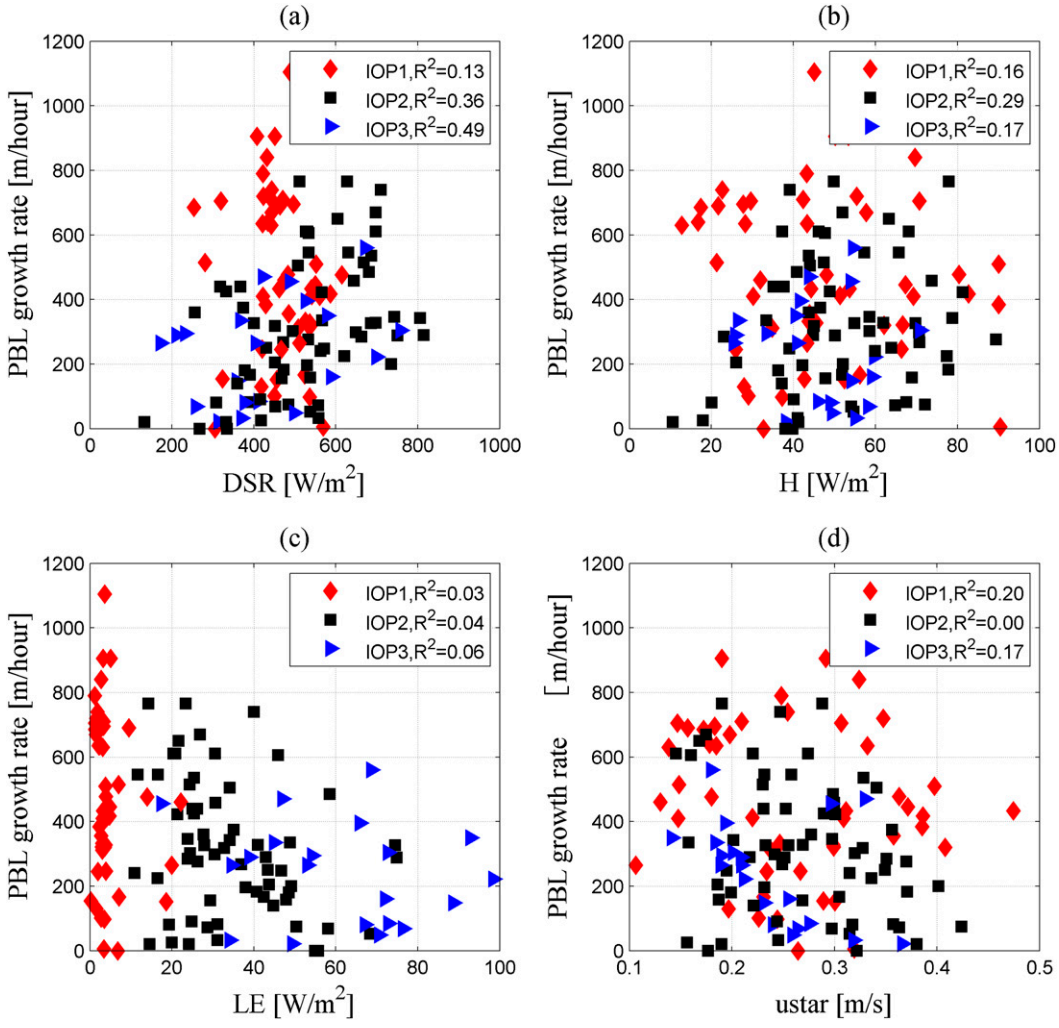

FIG. 3. Relation between PBL growth rate and (a) mean downward shortwave radiation (DSR), (b) surface sensible heat flux (H), (c) latent heat flux (LE), and (d) friction velocity ($U_\star$). The PBL growth rates for 0900–1300 and 0900–1900 were plotted against their corresponding mean surface variable values. The coefficient of determination from linear regression analysis, R^2, is listed in the legend.

moisture availability (competing for the energy for PBL growth) within any of the IOPs. Mechanical energy for PBL growth (assumed to be reflected in $U_\star$), finally, appears to be completely irrelevant at the present site.

During IOP3, however, the PBL appears to grow somewhat deeper when more radiative (shortwave) energy is available. It may therefore be concluded that indeed in summer (IOP3) over the TP the available surface energy is tentatively measured by (DSR − LE), and hence the state of the surface (SM) or H play a somewhat important role in determining the growth rate of the PBL at the present site.

When inspecting the differences among the IOPs, however, it is noted that stronger PBL growth is not associated with larger (radiative) energy input nor with stronger H. IOP1, when the truly deep PBLs are observed, is not characterized through the strongest DSR or H. Rather, the same range of surface heat flux (some 20–100 W m^{-2}) is associated with distinctly different PBL growth rates in the three IOPs. A small latent heat flux (and similarly soil moisture or large RH) is usually related to more energy being available for PBL growth. Indeed, the three IOPs exhibit distinctly different LE (and SM, not shown) and have correspondingly different PBL growth rates—but this is not reflected in the sensible heat fluxes (Fig. 3). If the reduced evaporation (drier conditions) during IOP1 were the key process to make all the available energy effective for PBL growth, this would have to be visible in the sensible heat flux (i.e., H would have to be large in IOP1 and smaller in IOP2 and IOP3).

It is therefore concluded that the surface data cannot explain the differences in PBL depth between the IOPs nor the differences within IOP1 when the particularly deep PBLs are observed. Other mechanisms than surface energy fluxes must consequently be responsible for the strong growth rate of the PBL over the TP in winter. These will further be explored in the following section.

c. *Idealized simulation of boundary layer energetics*

To investigate the key processes responsible for PBL growth over the TP, a sensitivity analysis with six simulations is performed using the BG91 model for ML growth on the basis of an example day during IOP1 (4 March 2008). Simulation A uses all available observations to specify the input parameters in order to assess whether the model is suitable for boundary layer growth over the TP. Simulation B then places the situation to sea level, while simulations C to F investigate the potential of enhanced mechanical turbulence, reduced density, enhanced surface sensible heat flux, and reduced overlying tropospheric stability—all relative to the sea level simulation B—to allow for a significantly deeper resulting PBL depth in the evening of the day.

Figure 4 depicts the modeled PBL depths as a function of time while Table 3 details the assumptions for the different simulations. As a control simulation (simulation A), observed surface heat fluxes and air density are used. Moreover, γ is determined using a 500-m-deep layer above the PBL top from the 0700 LT sounding for the integration between 0900 and 1300 LT and from the 1300 LT sounding for the remainder of the daytime. The following values are found: $\gamma \approx 0.0009\,\mathrm{K\,m^{-1}}$ for the initial period, $\gamma \approx 0.0011\,\mathrm{K\,m^{-1}}$ for the latter period, and $\gamma \approx 0.0017\,\mathrm{K\,m^{-1}}$ for the last hour (i.e., 1900–2000 LT) using the 1900 LT sounding.

In the "sea level" simulation (simulation B) the location is assumed to be at 1000 hPa, which results in a higher density of $\rho = 1.25\,\mathrm{kg\,m^{-3}}$. A standard free troposphere stability of $\gamma \approx 0.01\,\mathrm{K\,m^{-1}}$ is used (adopted from BG91). In the sensitivity simulations, $U_\star$ is enhanced by a factor of three (C), the actually observed density (at 4415 m MSL) is used (D), the sensible heat flux is enhanced by a factor of three (E), and the actually observed tropospheric stratification "over sea level" (F) is employed. To compare these simulations to the measured PBL depths, we assume that it took approximately 1 h for the 1900 LT radiosonde to travel through the troposphere; therefore, the final PBL depth is determined at 2000 LT. For all simulations, h_0 (the initial boundary layer height to start the simulation with; see section 2b) is set to 300 m based on the estimated stable boundary layer depth from the 0700 LT sounding on 4 March 2008. The actual boundary layer growth simulation is initiated at 0900 LT—that is, when the sensible heat flux first became positive.

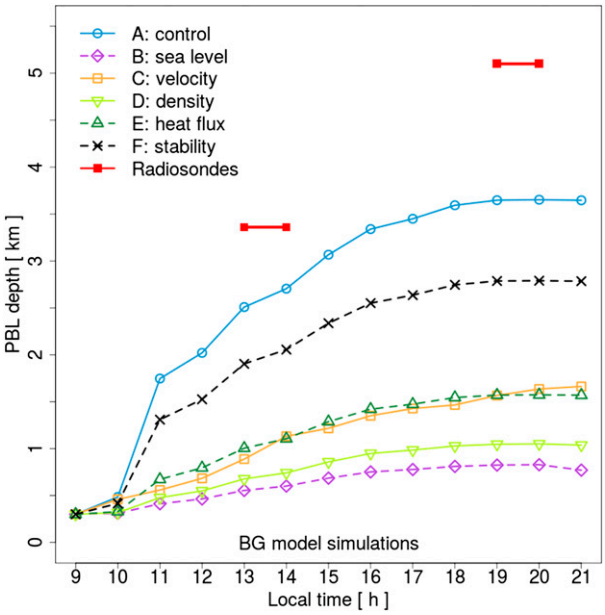

FIG. 4. Mixed-layer depths simulated with the BG91 slab model for six scenarios (see Table 3 and section 3c). The boundary layer depth at 0900 LT is assumed to be 300 m in all scenarios. Red horizontal line segments at 1300 and 1900 correspond to the radiosonde-retrieved PBL on 4 Mar 2008 (1 h approximately corresponds to the estimated time from launching the sounding to reaching the PBL top).

In the control run (simulation A) where all the input variables to the BG91 model are estimated from observations the resulting PBL is quite deep (3650 m). This is considerably smaller than the actually observed PBL depth (5055 m) because of the involved assumptions and simplifications. First, the model is highly idealized (one dimensional, some of the processes being parameterized). Second and most important, some of the crucial input variables (γ in particular) are not available continuously (and assumed constant between the soundings from which they are estimated). Still, we note that simulation A produced a deep PBL—both in absolute and relative terms—so that we conclude that the BG91 model possesses sufficient realism to investigate the sensitivities to the input variables, even if its amplitude may be underestimated for the present case.

Simulation B shows that the observed sensible heat and momentum fluxes cannot support a very deep PBL when ρ and λ are fixed to represent "average sea level conditions." Even after reducing density (simulation D) and enhancing the sensible heat flux (simulation E) or the momentum flux (to increase mechanical mixing, simulation C) by a factor of three, the ML depth does not grow substantially higher than the typical 1000 m.

TABLE 3. Variable settings and results for the sensitivity experiment with the BG91 model.

Simulation	Description	Reference height (m MSL)	$U_\star$ (m s^{-1})	ρ (kg m^{-3})	$\overline{w'\Theta_0'}$ (K m s^{-1})	γ (K m^{-1})	Base height h_{in} (m)	Hours at 1400 LT (m AGL)	Hours at 2000 LT (m AGL)
A	Observed (obs)	4415 (TP)	obs	obs	obs	obs	300	2700	3650
B	Reference, sea level	0 (sea level)	obs	1.25	obs	0.01	300	600	830
C	Impact of $U_\star$	0	3× enhanced	1.25	obs	0.01	300	1130	1635
D	Impact of ρ	4415	obs	obs	obs	0.01	300	740	1050
E	Impact of $w'\Theta_0'$	0	obs	1.25	3× enhanced	0.01	300	1110	1570
F	Impact of γ	0	obs	1.25	obs	obs	300	2060	2790

Therefore, the hypothesis that the low air density over the TP might be the reason for the deep PBL can be rejected.

The stability of the overlying free troposphere (γ), finally, produces an appreciably deep PBL when using the observed values as input and sea level conditions otherwise (simulation F). Deep PBLs can grow if either sufficiently strong surface forcing is available or the stability of the overlying (residual) layer, into which the PBL grows, is sufficiently weak so as to allow for an efficient entrainment (or both). If the former would be the dominant driver for the conditions of the wintertime western TP, simulation B with the observed heat and momentum fluxes (but situated at sea level) would have been expected to yield a considerably deep PBL in the first place. A strong sensitivity to thermal and mechanical forcing (simulations E and C, respectively) would have further supported a surface-forcing hypothesis. If the surface forcing (which is, in fact, relatively moderate) would be much more effective owing to the high altitude of the TP and the associated reduced density (Yang et al. 2004), simulation D would have exhibited a strong sensitivity. All this cannot be found from the idealized simulations with the BG91 model, so we conclude that the extraordinarily deep boundary layers over the TP cannot primarily be due to preferential surface-forcing conditions. On the other hand, the stability of the layer into which the ML grows (simulation F) exhibits a quite strong sensitivity—even for otherwise sea level conditions. This thus suggests that efficient entrainment due to weak stability aloft may be the key process for strong PBL growth under the conditions of the wintertime TP.

The importance of residual layer stability on the PBL growth has been discussed in the literature for some time and previous studies have shown that the potential temperature gradient above the convective boundary layer is an important parameter controlling the development of the PBL (Driedonks 1982; Gamo 1996; Fochesatto et al. 2001; Santanello et al. 2005; Villani et al. 2005; Chan and Wood 2013; Freire and Dias 2013; Blay-Carreras et al. 2014).

An analysis of the stability variations for the three IOPs reveals that relevant tropospheric vertical profiles (e.g., potential temperature and static and dynamic stability) are distinct during the three periods (not shown). For most of the days during IOP1 the observed lapse rate is very close to the dry adiabate for (at least) some 2 km above ground for both the 0700 and 1300 LT soundings. During IOP2 and IOP3, on the other hand, the lapse rate is typically assuming values around 5 K per 100 m (i.e., $-\delta T/\delta Z \approx 0.5\,\mathrm{K\,m^{-1}}$) within the first few hundred meters.

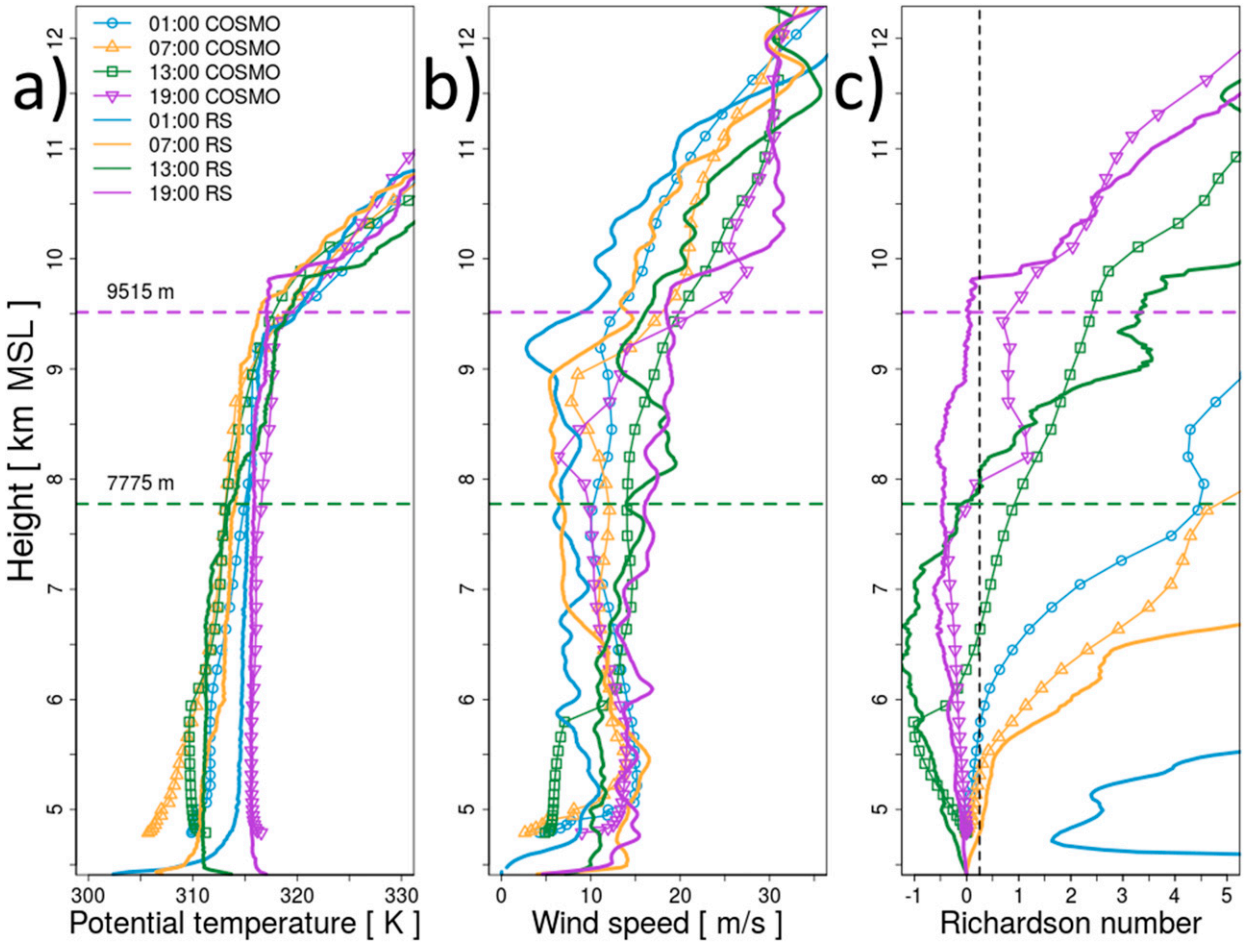

FIG. 5. Profiles of (a) potential temperature (K), (b) wind speed ($m\,s^{-1}$), and (c) the bulk Richardson number at 0100 LT (blue line, circles), 0700 LT (orange line, upward triangles), 1300 LT (green line, squares), and 1900 LT (purple line, downward triangles) on 4 Mar 2008 based on radiosonde (RS) observations and COSMO model simulations. The horizontal dashed lines show the tops of the PBL at 1300 (purple) and 1900 (green) as determined based on observational data (see section 2a).

From IOP1 to IOP3, the vertical distributions of the static and dynamic stability become less and less supportive for dry convection. The atmospheric stratification over the plateau during IOP1 is therefore more favorable for PBL growth, since entrainment at the top of the PBL is enhanced (Westra et al. 2012). These differences permit the PBL to grow much higher during IOP1 than during IOP2 or IOP3.

d. High-resolution simulation of a case study day

To further investigate the causes of variations in the stability and their relations with large-scale dynamical processes, COSMO is run for all three IOPs in 2008 (see section 2c). Figure 2 shows the time series of PBL depths determined from the observations, diagnosed from ERA-Interim data and simulated with COSMO. All three data sources agree that the deepest PBLs occurred during IOP1, followed by those during IOP2 and IOP3. This agreement provides confidence that the COSMO results reproduce the relevant processes leading to a very high PBL over high orography as observed from the Rs data. It is important to note that the COSMO model usually produces the highest PBL, especially for IOP2.

Figure 5 shows a comparison between the radiosonde observations and the COSMO simulation for a single day (4 March 2008). The observed MLs at 1300 and 1900 LT are characterized through conditions of forced convection ($\partial\Theta/\partial z \approx 0$, Fig. 5a, and scattered elevated shear layers, Fig. 5b) below the diagnosed ML heights of about 7.8 and 9.5 km, respectively. The profiles of Ri_B (Fig. 5c) suggest that this entire layer is essentially turbulent ($\mathrm{Ri}_B < 0.25$).

The COSMO simulations reveal qualitatively similar conditions, even if the diagnosed ML heights at 1300 and 1900 LT would be substantially lower (6.3 and 7.9 km, respectively, when using the parcel method and 6.7/8.0 km

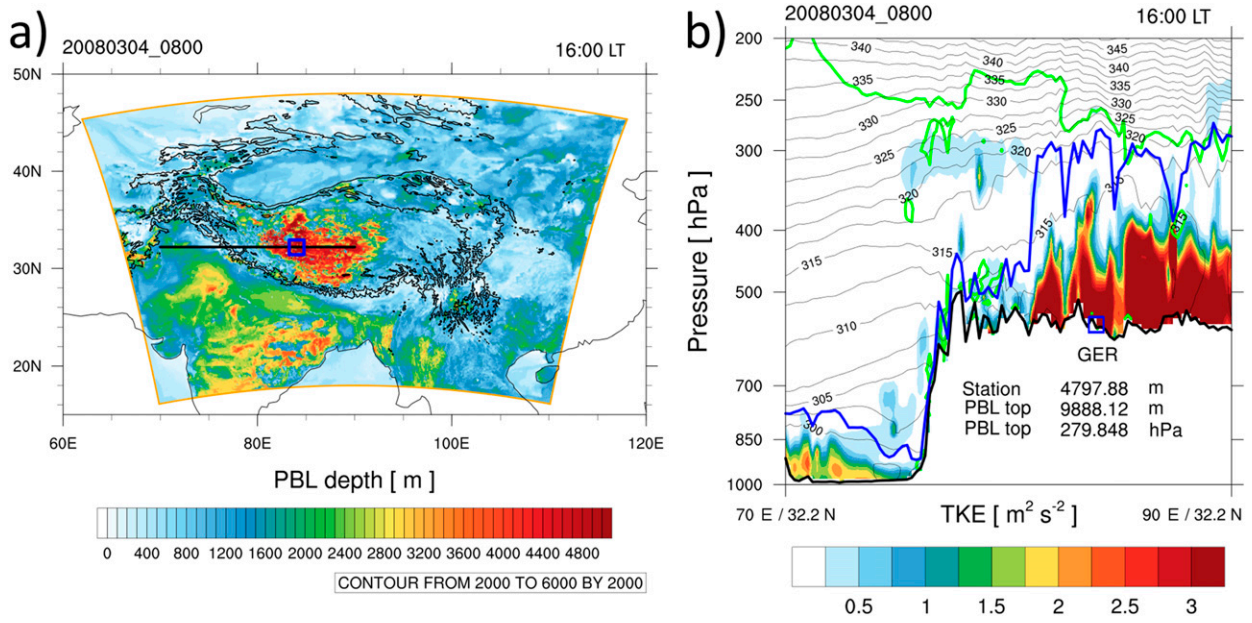

FIG. 6. (a) PBL depth (m) derived from the COSMO simulations over and around the Tibetan Plateau region, (b) vertical cross section at 1600 LT 4 Mar 2008 along the latitude of the Gerze station (32.2°N) from 70° to 90°E, as indicated by the horizontal line in (a). Displayed in (b) are TKE ($m^2 s^{-2}$, colored), PBL top determined using the bulk Richardson number method (blue line), isentropes (K, black thin lines), and the 2 PVU isoline (green) as reference for the dynamical tropopause. The thick black line in (b) shows the topography along 32.2°N/70°E to 32.2°N/90°E corresponding to the black line in (a).

based on the critical Richardson number). Figure 2, however, reveals that COSMO produces an equally deep PBL on this day, but the maximum depth is reached an hour earlier than observed.

Figure 6a shows the geographical distribution of the PBL depth around the TP as simulated by COSMO at 1600 LT on 4 March 2008. Large but spatially variable PBL depths (locally larger than 4000 m) are found over a relatively wide area around Gerze station. We also observe, however, that it is not "the TP as a whole" that hosts those extraordinarily deep PBLs. For the given day, large parts (especially in the east and west of the plateau) of the TP have boundary layers of more moderate depths as would be feasible from local energetics (see Fig. 4 and section 3c). In Fig. 6b, a zonally aligned vertical cross section (black line in Fig. 6a) at Gerzes latitude shows potential temperature, TKE, the PBL top (Ri_B criterion), and the dynamical tropopause derived from PV with a threshold of 2 PVU (1 PVU = $10^{-6} m^2 s^{-1} K kg^{-1}$). The PBL top extracted at the Gerze station grid point reaches 9888 m MSL and is indeed not too far away from the tropopause. The TKE color contour indicates that substantial parts of what is diagnosed as PBL by the Richardson number also exhibits significant turbulence, which apparently is produced/enforced by near-surface processes.

Thus the extraordinarily deep PBL as observed at Gerze station essentially bears the characteristics of a turbulent boundary layer. The upper part, however, of the well-mixed layer (note the potential temperature contour over the plateau) has substantially reduced TKE. Similar to the PBL height itself, the boundary layer's upper portion exhibiting reduced TKE is spatially highly variable and seems to respond to some degree to the variability in surface elevation. This reduced TKE would suggest that the upper part of the well-mixed layer (i.e., the PBL) is influenced by top-down processes to a larger degree in this environment than what the classical model (for which the BG91 model might be taken as an idealized example) yields.

We also extract a TKE-derived PBL depth (not shown), which we define as the height at which TKE drops below 0.1 times the average value in the lowest five model levels (in each column). This TKE-derived boundary layer depth is not as high as that based on the Ri_B criterion, indicating that the uppermost part of the PBL (as determined by the Ri_B criterion) has significantly lower TKE than the lower part.

Overall, the COSMO simulation for an example day during IOP1 demonstrates that the model is able to capture the vertical structure of the PBL over the TP (Fig. 5) and that this vertical structure is that of a turbulent boundary layer (Fig. 6)—that is, over large parts characterized through substantial TKE. Furthermore the simulation reveals that PBL depth is

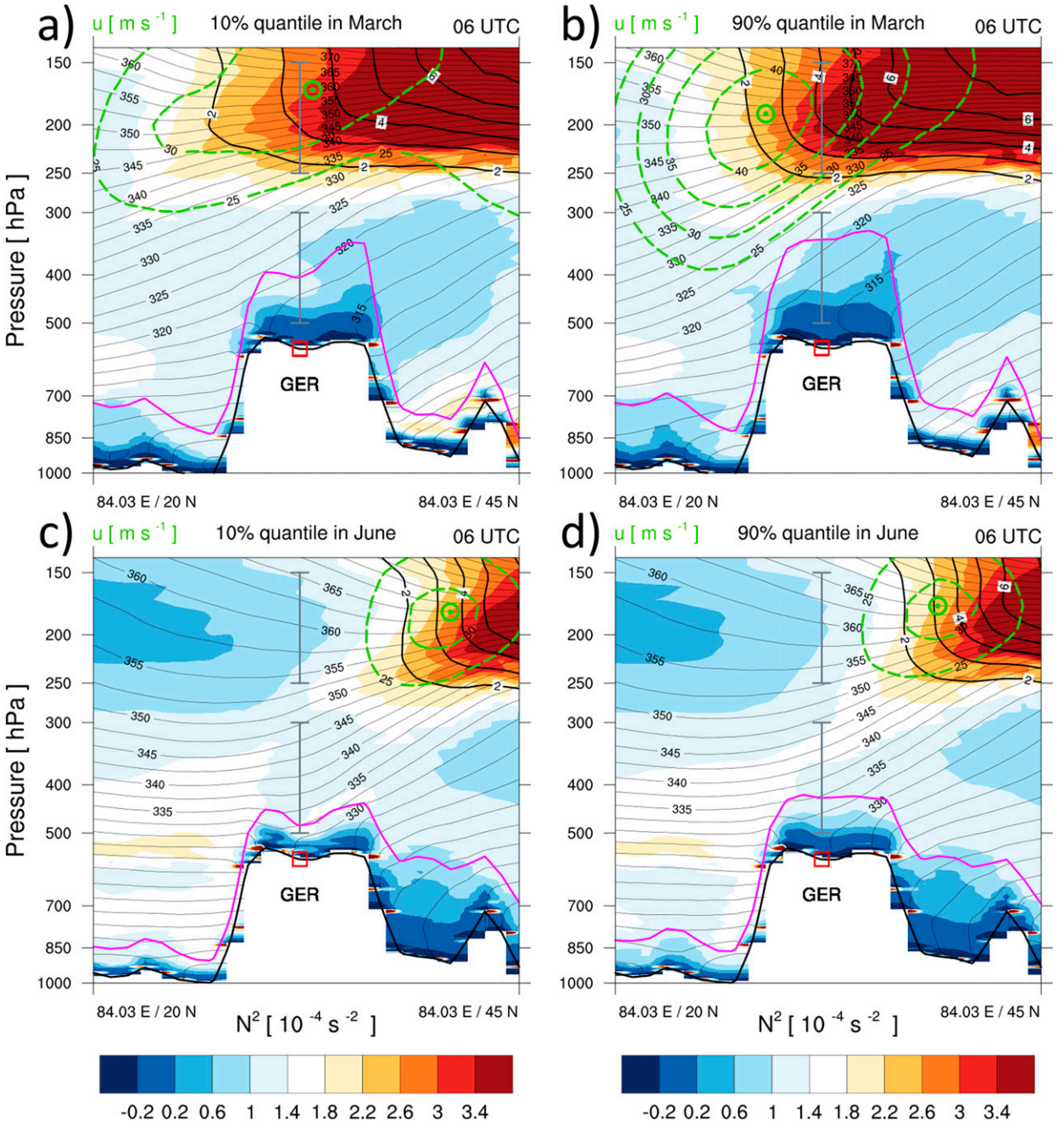

FIG. 7. Meridional cross-section composites of (left) low-PBL days (PBL depth < 10% quantile) and (right) high-PBL days (PBL depth > 90% quantile) in (top) March and (bottom) June based on ERA-Interim data at 0600 UTC between 2000 and 2011. The cross sections are aligned meridionally from 20° to 45°N at the longitude of GER station (84.03°E). Displayed are the Brunt–Väisälä frequency N^2 (10^{-4} s^{-2}, colored), PBL top (purple line), zonal wind speeds exceeding 25 m s^{-1} (green dashed contours, contour interval 5 m s^{-1}), wind maximum (green dotted circle), isentropes (K, thin black lines), and the isolines of potential vorticity (>2 PVU, black lines, contour interval 1 PVU). The location of Gerze station (GER) is indicated by a red square. Gray vertical line segments illustrate the layers from 500 to 300 hPa and from 250 to 150 hPa used for the statistical analysis shown in Fig. 9. The black line denotes the topography along the meridional cross section.

spatially highly variable and—at least on the chosen day—confined to the western TP. To relate this spatial pattern to large-scale dynamical conditions of the upper troposphere/lower stratosphere, we now turn to the analysis of ERA-Interim (climatological) data, which has previously (Fig. 2) been demonstrated to be in good accordance with both COSMO and observations.

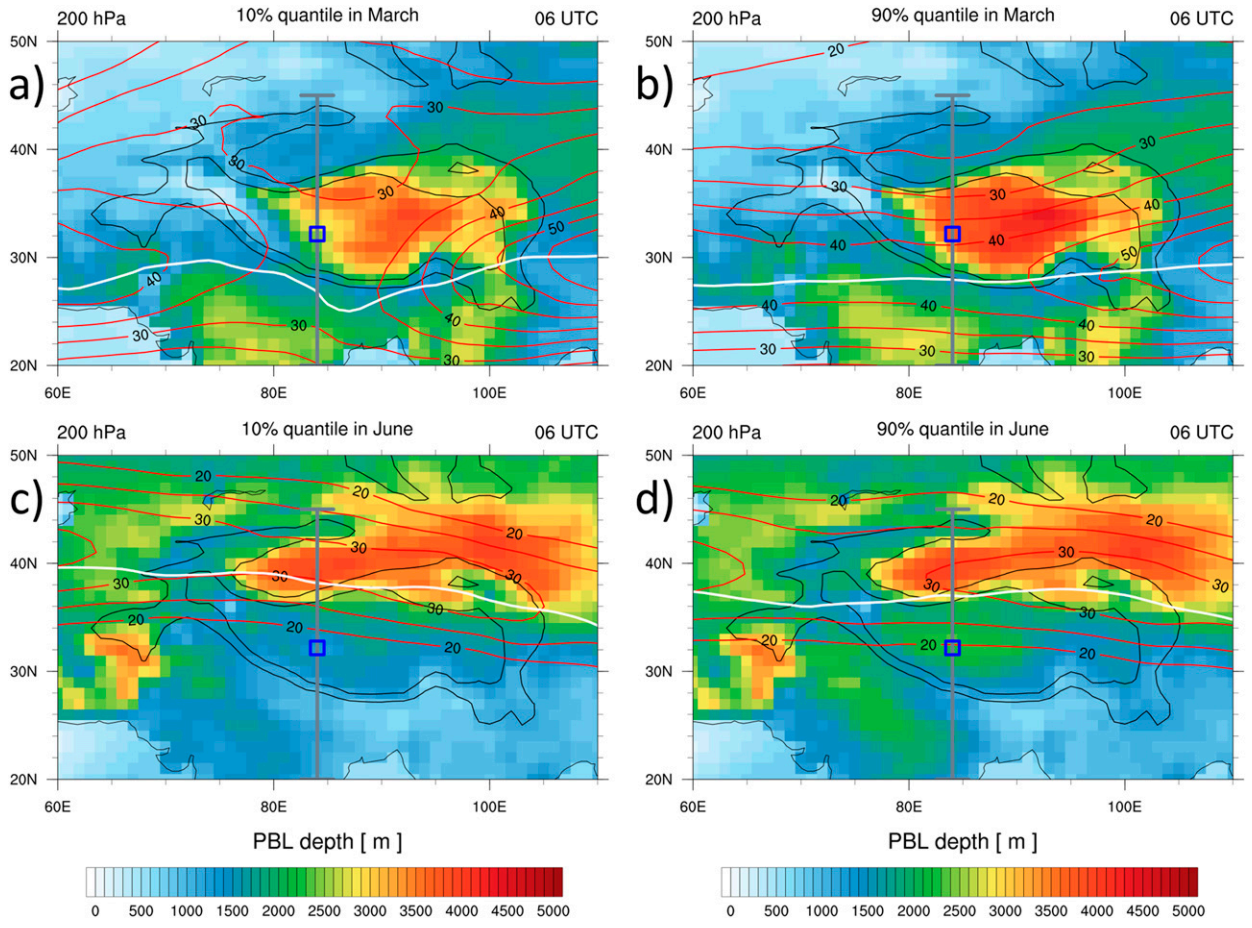

FIG. 8. Composites of (left) low-PBL days (PBL depth < 10% quantile) and (right) high-PBL days (PBL depth > 90% quantile) in (top) March and (bottom) June based on ERA-Interim data at 0600 UTC between 2000 and 2011. Displayed are the PBL depth (m, colored), orography (black lines, contour interval 2000 m), zonal wind speed at 200 hPa ($m\,s^{-1}$, red lines), and dynamical tropopause (2 PVU) at 200 hPa (white line). The meridionally aligned gray lines illustrate the location of the cross sections shown in Fig. 7.

e. ERA-Interim composites

To find systematic differences between days with low PBLs and days with high PBLs, we compiled a 12-yr climatology based on ERA-Interim data from 2000 to 2011 (see also Fig. 1). Because the PBL is highest in the afternoon, the 0600 UTC analysis is used, which corresponds to 1400 LT.

In Fig. 7, we show composites of meridionally aligned vertical cross sections (at Gerze's longitude, between 20° and 45°N) at 0600 UTC. Displayed are composites for days in March (representative of IOP1, top row) and June (IOP2, bottom row) with PBL height lower than the 10% quantile (left column) and higher than the 90% quantile (right column), thus depicting typical conditions when the PBL is particularly low and high, respectively. Each composite thus consists of approximately 36 analysis times between 2000 and 2011.

Figure 7 shows that in both months, the atmosphere above the plateau is characterized by lower stability (smaller N^2, where N is the Brunt–Väisälä frequency) on days with high PBLs (heights exceeding the 90% quantile) than on days with low PBLs (lowest 10%). This finding is consistent with our previous analysis of the radio soundings and the result of the sensitivity study using the BG91 model, namely that a weakly stratified free troposphere favors the development of a deep PBL. The fact that Gerze station appears to be a local minimum in the PBL depth for the days with shallow PBL is a consequence of the meridional variation in topography.

The upper-level structure in March clearly differs between low-PBL and high-PBL days. On days with high PBLs, the jet stream features higher wind speeds ($\approx$45 $m\,s^{-1}$ compared to $\approx$35 $m\,s^{-1}$ for low PBLs) and is located farther to the south. This is reflected in the PV distribution, as can be seen from the labeled

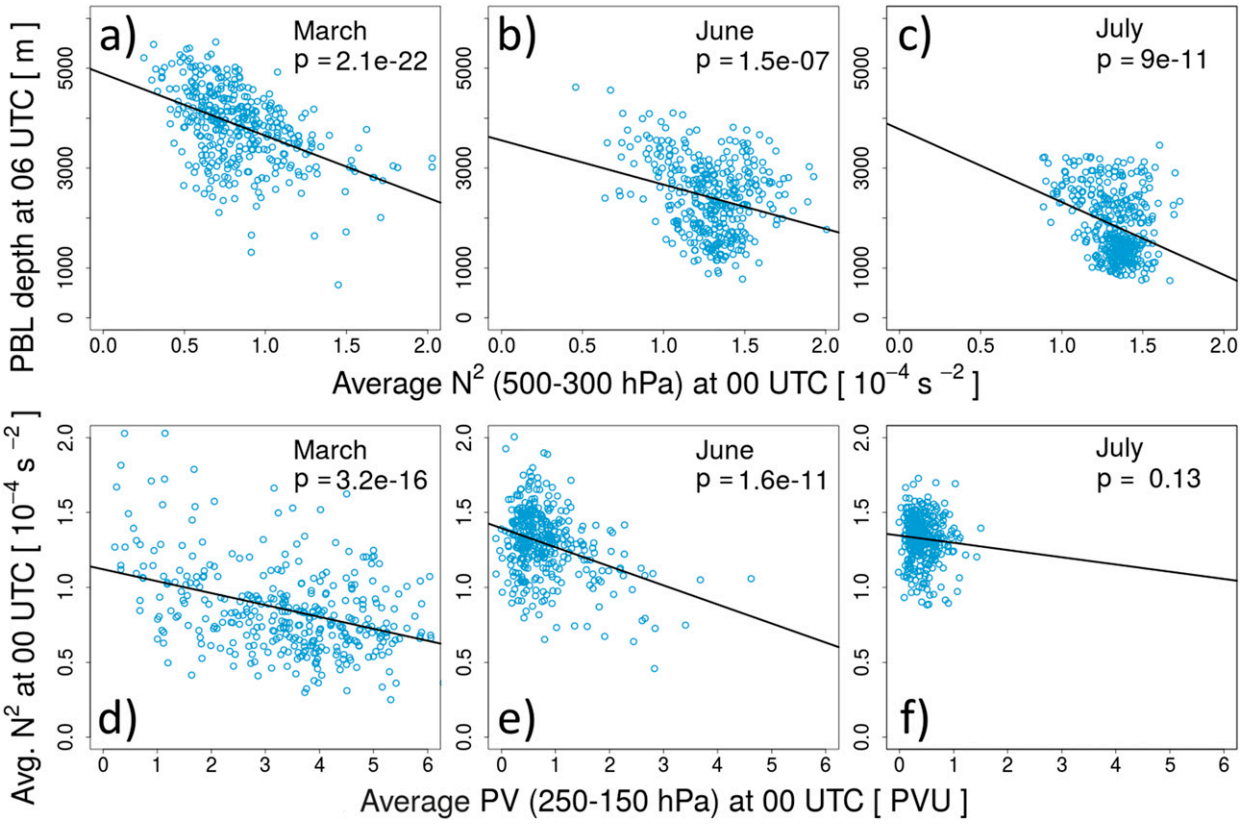

FIG. 9. Monthly plots of (a)–(c) PBL depth at 0600 UTC (m) over Gerze station plotted vs stability at 0000 UTC (N^2, $10^{-4}\,s^{-2}$) averaged between 500 and 300 hPa in the vertical column above the station (see lower gray line segment in Fig. 7) and (d)–(f) N^2 (same units, same average) at 0000 UTC vs PV averaged between 250 and 150 hPa at 0000 UTC (see upper gray line segment in Fig. 7), based on ERA-Interim data between 2000 and 2011. The black lines shows a linear regression fit with the p value indicating the statistical significance.

contours in Fig. 7 (2 to 7 PVU), and it is quite obvious from the stronger longitudinal gradient of N^2 in the stratosphere for the high-PBL days. In June, both the low- and high-PBL days are characterized by a jet that is weak (even weaker than the low-PBL days in March) and located far to the north of Gerze station's latitude. Correspondingly low PV is observed over the western TP and also the stratification of the troposphere is considerably stronger than in March. It thus appears that the weak stratification aloft that is essential for an efficient entrainment process and hence strong PBL growth is associated with a strong jet at a relatively low latitude and thus a positive PV anomaly above Gerze station. The more the influence of the PV anomaly aloft is reduced (i.e., the jet is displaced to the north) the smaller is the potential for PBL growth due to reduced stability.

The horizontal structure of the jet stream over the TP region can be seen from Fig. 8 (depicted at 200 hPa). Pronounced differences between low- and high-PBL days are especially visible in March. The jet is not only stronger on days with high PBLs but is also more zonally uniform than during days with low PBLs. This difference is also reflected in the shape of the 2 PVU isoline at 200 hPa (white line). In June, there are only slight differences at 200 hPa between the high- and low-PBL days.

To investigate the influence of the upper-level structure on PBL height more systematically, we extract N^2 averaged between 500 and 300 hPa (lower gray line segment in Fig. 7) and PV averaged between 250 and 150 hPa (upper gray line segment in Fig. 7) for both the 0000 and 0600 UTC analysis times between 2000 and 2011.

The top row in Fig. 9 shows scatterplots of PBL depth at 0600 UTC (afternoon, LT) versus N^2 at 0000 UTC (morning, LT) for March, June, and July. Clearly, there is a very significant (p values from linear regression below 10^{-7}) correlation between high PBLs and low stability 6 h before. This further supports the findings from the BG91 model that the stability of the layer into which the PBL grows plays a crucial role for PBL development over the TP (cf. section 3c). By visually inspecting the plots, one can see that in March, the linear regression is strongly influenced by a few points with high N^2 and comparatively low-PBL depth, i.e., the

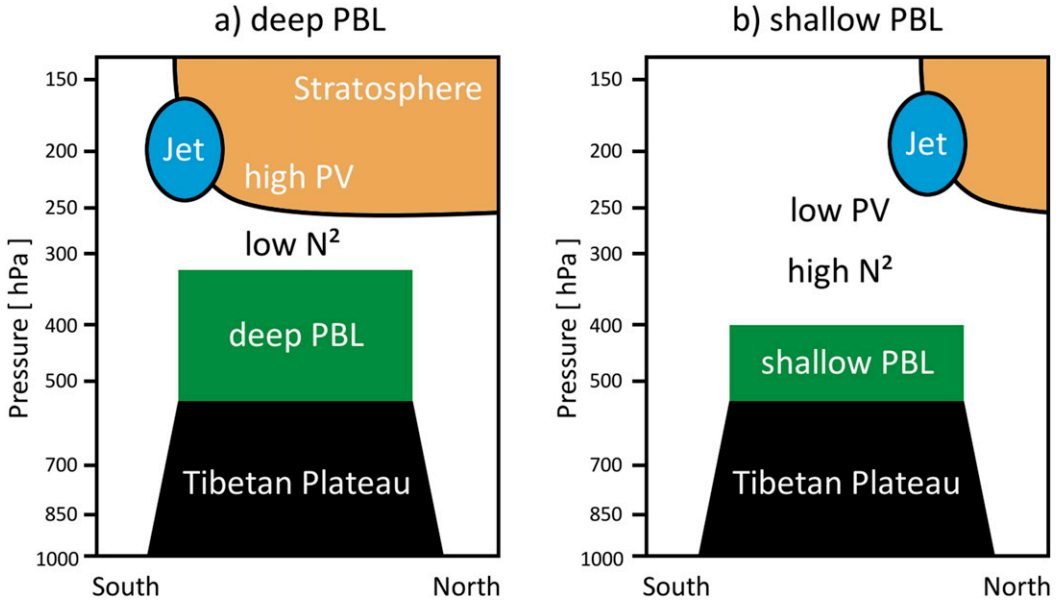

FIG. 10. Schematic figure of the PBL above the Tibetan Plateau for (a) deep PBL cases (winter) and (b) shallow PBL cases (summer).

actual relation between these two variables could be even stronger (the same is true for June).

Following up on the results shown in Fig. 7, we further display the relation between the averaged stability above the plateau and averaged upper-level PV in the bottom row of Fig. 9. Here as well very significant correlations between low stability over the plateau and high upper-level PV are found in March and June (p values below 10^{-11}). In July, upper-level PV is apparently quite reduced reflecting the displacement of the jet toward the north and its variability is not clearly related to stability over the plateau (p value of 0.13). The relation of upper-level PV with stability can be understood in the PV framework. Based on idealized simulations, Hoskins et al. (1985) demonstrated that a positive upper-level PV anomaly is associated with a destabilization of the air masses below (lifted and spread-out isentropes, their Fig. 15). Thus, it appears that the more southern jet position in late winter (i.e., March or IOP1) is situated just about ''optimal'' relative to the western TP so that the location of the strong PV aloft (interpreted as the positive PV anomaly here) is associated with a weak stratification over the area of the western TP and hence allows for efficient entrainment resulting in the corresponding deep PBL.

4. Summary and discussion

Our observations show that a deep near-neutral layer in the upper troposphere prevails over the TP in the winter season. Owing to the high elevation of the TP (which has an average elevation of 4 km), the PBL top above the plateau approaches the upper troposphere and lower stratosphere (Chen et al. 2013; Škerlak et al. 2014), with important implications for atmospheric chemistry and the transport of polluted air masses.

Previous studies have shown that deep mixed layers develop to high altitudes when the daytime mixed layer becomes linked to a weakly stratified, near-neutral layer above the mixed layer (Gamo 1996; Han et al. 2012). We confirm this finding and show, using comparison to measurements at the surface and an idealized slab model, that this low stability is indeed the crucial factor leading to strong PBL growth over the TP in winter. The relatively strong nighttime plateau surface cooling furthermore leads to a deep residual layer that is isolated from the surface during the night and eroded during the development of the following day's ML thus giving rise to a deep turbulent boundary layer. With the development of the monsoon in summertime, however, the nighttime deep residual layer disappears and generally larger vertical temperature gradients aloft lead to higher stability and thus limit PBL growth. The PBL depth is then comparable to that usually observed over lowland areas.

We finally provide statistical evidence for an important influence of upper-level structures on PBL growth based on 12 yr of ERA-Interim data. More specifically, we find that days with high-ranging PBLs over the TP and thus low stability aloft are associated

with high values of PV 6 h earlier. Relatively shallow PBLs over the TP, on the other hand, with strong stability aloft are associated with low values of PV. An interpretation of these statistical results can be found from the PV framework in which it can be demonstrated that strong upper-level PV (a positive PV anomaly) is associated with reduced stability below (Hoskins et al. 1985).

PBL tops reaching heights over 9 km (MSL) are certainly favored by the elevated topography of the TP (>4 km MSL). An extraordinarily deep boundary layer (>5 km depth) necessary for allowing its top to reach the upper troposphere/lower stratosphere, however, is shown to be due to a combination of dynamic factors. If the jet is strong and lies to the south of the TP (as typically the case in March on days with deep PBLs) large upper-level PV and strong baroclinicity can be found over the plateau. This then is associated with a relatively weakly stratified atmosphere over the plateau as it is characteristic for a positive upper-level PV anomaly (Hoskins et al. 1985). This weak stratification of the layer into which the boundary layer grows allows it to become very deep and to reach depths that usually would not be reached given the available thermal (and mechanical) energy for boundary layer growth at the surface. In summer, on the other hand, when typically deep boundary layers are observed in other regions of the world, the upper-level jet position is much farther to the north of the TP (and the jet is weaker), so that the reduced stability over the plateau is not found and the boundary layer only grows to the "typical" 1–2 km AGL. These two situations are schematically sketched in Fig. 10.

Acknowledgments. We acknowledge the support of the Chinese National Natural Science Foundation (41175008), EU-FP7 CEOPAEGIS (212921), EU-FP7 CORE-CLIMAX (313085), and the China Exchange Programme (13CDP007) project. Juan A. Añel is supported by a Ramón y Cajal Fellowship funded by the Ministry of Economy and Competitiveness of the Government of Spain (RYC-2013-14560). The authors thank all of the participants from China and Japan for their work collecting the JICA Tibetan Plateau meteorological observations. Prof. Xiangde Xu and Prof. Toshio Koike are acknowledged for their coordination of the Sino-Japan JICA project.

REFERENCES

Ao, C. O., D. E. Waliser, S. K. Chan, J.-L. Li, B. Tian, F. Xie, and A. J. Mannucci, 2012: Planetary boundary layer heights from GPS radio occultation refractivity and humidity profiles. *J. Geophys. Res.*, **117**, D16117, doi:10.1029/2012JD017598.

Baklanov, A. A., and Coauthors, 2011: The nature, theory, and modeling of atmospheric planetary boundary layers. *Bull. Amer. Meteor. Soc.*, **92**, 123–128, doi:10.1175/2010BAMS2797.1.

Baldauf, M., A. Seifert, J. Förstner, D. Majewski, M. Raschendorfer, and T. Reinhardt, 2011: Operational convective-scale numerical weather prediction with the COSMO model: Description and sensitivities. *Mon. Wea. Rev.*, **139**, 3887–3905, doi:10.1175/MWR-D-10-05013.1.

Batchvarova, E., and S.-E. Gryning, 1991: Applied model for the growth of the daytime mixed layer. *Bound.-Layer Meteor.*, **56**, 261–274, doi:10.1007/BF00120423.

Blay-Carreras, E., and Coauthors, 2014: Role of the residual layer and large-scale subsidence on the development and evolution of the convective boundary layer. *Atmos. Chem. Phys.*, **14**, 4515–4530, doi:10.5194/acp-14-4515-2014.

Boos, W. R., and Z. Kuang, 2010: Dominant control of the South Asian monsoon by orographic insulation versus plateau heating. *Nature*, **463**, 218–222, doi:10.1038/nature08707.

Chan, K. M., and R. Wood, 2013: The seasonal cycle of planetary boundary layer depth determined using COSMIC radio occultation data. *J. Geophys. Res. Atmos.*, **118**, 12 422–12 434, doi:10.1002/2013JD020147.

Chen, X., 2013: The plateau scale land–air interaction and its connections to troposphere and lower stratosphere. Ph.D. dissertation, University of Twente, 164 pp. [Available online at https://www.itc.nl/library/papers_2013/phd/chen.pdf.]

——, J. A. Añel, Z. Su, L. de la Torre, H. Kelder, J. van Peet, and Y. Ma, 2013: The deep atmospheric boundary layer and its significance to the stratosphere and troposphere exchange over the Tibetan Plateau. *PLoS ONE*, **8**, e56909, doi:10.1371/journal.pone.0056909.

Cuesta, J., and Coauthors, 2008: Multiplatform observations of the seasonal evolution of the Saharan atmospheric boundary layer in Tamanrasset, Algeria, in the framework of the African Monsoon Multidisciplinary Analysis field campaign conducted in 2006. *J. Geophys. Res.*, **113**, D00C07, doi:10.1029/2007JD009417.

Dee, D. P., and Coauthors, 2011: The ERA-Interim reanalysis: Configuration and performance of the data assimilation system. *Quart. J. Roy. Meteor. Soc.*, **137**, 553–597, doi:10.1002/qj.828.

Driedonks, A., 1982: Models and observations of the growth of the atmospheric boundary layer. *Bound.-Layer Meteor.*, **23**, 283–306, doi:10.1007/BF00121117.

Eltahir, E. A., 1998: A soil moisture–rainfall feedback mechanism: 1. Theory and observations. *Water Resour. Res.*, **34**, 765–776, doi:10.1029/97WR03499.

Endo, S., T. Shinoda, T. Hiyama, H. Uyeda, K. Nakamura, H. Tanaka, and K. Tsuboki, 2008: Characteristics of vertical circulation in the convective boundary layer over the Huaihe River basin in China in the early summer of 2004. *J. Appl. Meteor. Climatol.*, **47**, 2911–2928, doi:10.1175/2008JAMC1769.1.

Fan, S., Q. Fan, W. Yu, X. Luo, B. Wang, L. Song, and K. Leong, 2011: Atmospheric boundary layer characteristics over the Pearl River Delta, China, during the summer of 2006: Measurement and model results. *Atmos. Chem. Phys.*, **11**, 6297–6310, doi:10.5194/acp-11-6297-2011.

Fochesatto, G. J., P. Drobinski, C. Flamant, D. Guedalia, C. Sarrat, P. H. Flamant, and J. Pelon, 2001: Evidence of dynamical coupling between the residual layer and the developing convective boundary layer. *Bound.-Layer Meteor.*, **99**, 451–464, doi:10.1023/A:1018935129006.

Freire, L. S., and N. L. Dias, 2013: Residual layer effects on the modeling of convective boundary layer growth rates with a

slab model using FIFE data. *J. Geophys. Res. Atmos.*, **118**, 12 869–12 878, doi:10.1002/jgrd.50796.

Gamo, M., 1996: Thickness of the dry convection and large-scale subsidence above deserts. *Bound.-Layer Meteor.*, **79**, 265–278, doi:10.1007/BF00119441.

Han, B., S. Lü, and Y. Ao, 2012: Development of the convective boundary layer capping with a thick neutral layer in Badanjilin: Observations and simulations. *Adv. Atmos. Sci.*, **29**, 177–192, doi:10.1007/s00376-011-0207-4.

Hecht, J., and Coauthors, 2004: An overview of observations of unstable layers during the Turbulent Oxygen Mixing Experiment (TOMEX). *J. Geophys. Res.*, **109**, D02S01, doi:10.1029/2002JD003123.

Hennemuth, B., and A. Lammert, 2006: Determination of the atmospheric boundary layer height from radiosonde and lidar backscatter. *Bound.-Layer Meteor.*, **120**, 181–200, doi:10.1007/s10546-005-9035-3.

Högström, U., 1996: Review of some basic characteristics of the atmospheric surface layer. *Bound.-Layer Meteor.*, **78**, 215–246, doi:10.1007/BF00120937.

Holzworth, G. C., 1964: Estimates of mean maximum mixing depths in the contiguous United States. *Mon. Wea. Rev.*, **92**, 235–242, doi:10.1175/1520-0493(1964)092<0235:EOMMMD>2.3.CO;2.

——, 1967: Mixing depths, wind speeds and air pollution potential for selected locations in the United States. *J. Appl. Meteor.*, **6**, 1039–1044, doi:10.1175/1520-0450(1967)006<1039:MDWSAA>2.0.CO;2.

Hoskins, B. J., M. E. McIntyre, and A. W. Robertson, 1985: On the use and significance of isentropic potential vorticity maps. *Quart. J. Roy. Meteor. Soc.*, **111**, 877–946, doi:10.1002/qj.49711147002.

Korhonen, K., and Coauthors, 2014: Atmospheric boundary layer top height in South Africa: Measurements with lidar and radiosonde compared to three atmospheric models. *Atmos. Chem. Phys.*, **14**, 4263–4278, doi:10.5194/acp-14-4263-2014.

Kursinski, E. R., G. A. Hajj, J. T. Schofield, R. P. Linfield, and K. R. Hardy, 1997: Observing Earth's atmosphere with radio occultation measurements using the global positioning system. *J. Geophys. Res.*, **102**, 23 429–23 465, doi:10.1029/97JD01569.

Li, M., Y. Dai, Y. Ma, L. Zhong, and S. Lu, 2006: Analysis on structure of atmospheric boundary layer and energy exchange of surface layer over Mount Qomolangma region (in Chinese). *Plateau Meteor.*, **25**, 807–813.

Li, Y., and W. Gao, 2007: Atmospheric boundary layer circulation on the eastern edge of the Tibetan Plateau, China, in summer. *Arct. Antarct. Alp. Res.*, **39**, 708–713, doi:10.1657/1523-0430(07-504)[LI]2.0.CO;2.

Luo, H., and M. Yanai, 1984: The large-scale circulation and heat sources over the Tibetan Plateau and surrounding areas during the early summer of 1979. Part II: Heat and moisture budgets. *Mon. Wea. Rev.*, **112**, 966–989, doi:10.1175/1520-0493(1984)112<0966:TLSCAH>2.0.CO;2.

McGrath-Spangler, E. L., and A. S. Denning, 2013: Global seasonal variations of midday planetary boundary layer depth from *CALIPSO* space-borne lidar. *J. Geophys. Res. Atmos.*, **118**, 1226–1233, doi:10.1002/jgrd.50198.

——, and A. Molod, 2014: Comparison of GEOS-5 AGCM planetary boundary layer depths computed with various definitions. *Atmos. Chem. Phys.*, **14**, 6717–6727, doi:10.5194/acp-14-6717-2014.

Nath, D., M. Venkat Ratnam, A. Patra, B. Krishna Murthy, B. Rao, and S. Vijaya, 2010: Turbulence characteristics over tropical station Gadanki (13.5°N, 79.2°E) estimated using high-resolution GPS radiosonde data. *J. Geophys. Res.*, **115**, D07102, doi:10.1029/2009jd012347.

Nyeki, S., and Coauthors, 2000: Convective boundary layer evolution to 4 km asl over high-alpine terrain: Airborne lidar observations in the Alps. *Geophys. Res. Lett.*, **27**, 689–692, doi:10.1029/1999GL010928.

Raman, S., and Coauthors, 1990: Structure of the Indian southwesterly pre-monsoon and monsoon boundary layers: Observations and numerical simulation. *Atmos. Environ.*, **24A**, 723–734, doi:10.1016/0960-1686(90)90273-P.

Rotach, M. W., and D. Zardi, 2007: On the boundary-layer structure over highly complex terrain: Key findings from MAP. *Quart. J. Roy. Meteor. Soc.*, **133**, 937–948, doi:10.1002/qj.71.

Sanchez-Mejia, Z. M., and S. A. Papuga, 2014: Observations of a two-layer soil moisture influence on surface energy dynamics and planetary boundary layer characteristics in a semiarid shrubland. *Water Resour. Res.*, **50**, 306–317, doi:10.1002/2013WR014135.

Santanello, J. A., Jr., M. A. Friedl, and W. P. Kustas, 2005: An empirical investigation of convective planetary boundary layer evolution and its relationship with the land surface. *J. Appl. Meteor.*, **44**, 917–932, doi:10.1175/JAM2240.1.

Seibert, P., F. Beyrich, S.-E. Gryning, S. Joffre, A. Rasmussen, and P. Tercier, 2000: Review and intercomparison of operational methods for the determination of the mixing height. *Atmos. Environ.*, **34**, 1001–1027, doi:10.1016/S1352-2310(99)00349-0.

Seidel, D. J., C. O. Ao, and K. Li, 2010: Estimating climatological planetary boundary layer heights from radiosonde observations: Comparison of methods and uncertainty analysis. *J. Geophys. Res.*, **115**, D16113, doi:10.1029/2009jd013680.

——, Y. Zhang, A. Beljaars, J.-C. Golaz, A. R. Jacobson, and B. Medeiros, 2012: Climatology of the planetary boundary layer over the continental United States and Europe. *J. Geophys. Res.*, **117**, D17106, doi:10.1029/2012jd018143.

Simmons, A., S. Uppala, D. Dee, and S. Kobayashi, 2007: ERA-Interim: New ECMWF reanalysis products from 1989 onwards. *ECMWF Newsletter*, No. 110, ECMWF, Reading, United Kingdom, 25–35. [Available online at http://www.ecmwf.int/sites/default/files/elibrary/2006/14615-newsletter-no110-winter-200607.pdf.]

Škerlak, B., M. Sprenger, and H. Wernli, 2014: A global climatology of stratosphere–troposphere exchange using the ERA-Interim data set from 1979 to 2011. *Atmos. Chem. Phys.*, **14**, 913–917, doi:10.5194/acp-14-913-2014.

Stull, R. B., 1988: *An Introduction to Boundary Layer Meteorology*. Kluwer Academic, 666 pp.

Sun, F., Y. Ma, M. Li, W. Ma, H. Tian, and S. Metzger, 2007: Boundary layer effects above a Himalayan valley near Mount Everest. *Geophys. Res. Lett.*, **34**, L08808, doi:10.1029/2007gl029484.

Szintai, B., P. Kaufmann, and M. W. Rotach, 2009: Deriving turbulence characteristics from the COSMO numerical weather prediction model for dispersion applications. *Adv. Sci. Res.*, **3**, 79–84, doi:10.5194/asr-3-79-2009.

Takemi, T., 1999: Structure and evolution of a severe squall line over the arid region in northwest China. *Mon. Wea. Rev.*, **127**, 1301–1309, doi:10.1175/1520-0493(1999)127<1301:SAEOAS>2.0.CO;2.

Tao, S.-Y., and Y.-H. Ding, 1981: Observational evidence of the influence of the Qinghai-Xizang (Tibet) Plateau on the occurrence of heavy rain and severe convective storms in China. *Bull. Amer. Meteor. Soc.*, **62**, 23–30, doi:10.1175/1520-0477(1981)062<0023:OEOTIO>2.0.CO;2.

Troen, I., and L. Mahrt, 1986: A simple model of the atmospheric boundary layer; sensitivity to surface evaporation. *Bound.-Layer Meteor.*, **37**, 129–148, doi:10.1007/BF00122760.

Ueno, K., S. Sugimoto, H. Tsutsui, K. Taniguchi, Z. Hu, and S. Wu, 2012: Role of patchy snow cover on the planetary boundary layer structure during late winter observed in the central Tibetan Plateau. *J. Meteor. Soc. Japan*, **90C**, 145–155, doi:10.2151/jmsj.2012-C10.

Villani, M. G., A. Maurizi, and F. Tampieri, 2005: Discussion and applications of slab models of the convective boundary layer based on turbulent kinetic energy budget parameterisations. *Bound.-Layer Meteor.*, **114**, 539–556, doi:10.1007/s10546-004-1415-6.

Vogelezang, D., and A. Holtslag, 1996: Evaluation and model impacts of alternative boundary-layer height formulations. *Bound.-Layer Meteor.*, **81**, 245–269, doi:10.1007/BF02430331.

von Engeln, A., and J. Teixeira, 2013: A planetary boundary layer height climatology derived from ECMWF reanalysis data. *J. Climate*, **26**, 6575–6590, doi:10.1175/JCLI-D-12-00385.1.

——, ——, J. Wickert, and S. A. Buehler, 2005: Using CHAMP radio occultation data to determine the top altitude of the planetary boundary layer. *Geophys. Res. Lett.*, **32**, L06815, doi:10.1029/2004GL022168.

Westra, D., G. Steeneveld, and A. Holtslag, 2012: Some observational evidence for dry soils supporting enhanced relative humidity at the convective boundary layer top. *J. Hydrometeor.*, **13**, 1347–1358, doi:10.1175/JHM-D-11-0136.1.

Wetzel, P. J., 1982: Toward parameterization of the stable boundary layer. *J. Appl. Meteor.*, **21**, 7–13, doi:10.1175/1520-0450(1982)021<0007:TPOTSB>2.0.CO;2.

Whiteman, C. D., 1990: Observations of thermally developed wind systems in mountainous terrain. *Atmospheric Processes over Complex Terrain*, *Meteor. Monogr.*, No. 45, Amer. Meteor. Soc., 5–42.

——, S. Zhong, X. Bian, J. Fast, and J. C. Doran, 2000: Boundary layer evolution and regional-scale diurnal circulations over the and Mexican plateau. *J. Geophys. Res.*, **105**, 10 081–10 102, doi:10.1029/2000JD900039.

Wu, G., Y. Liu, B. He, Q. Bao, A. Duan, and F.-F. Jin, 2012: Thermal controls on the Asian summer monsoon. *Sci. Rep.*, **2**, 404, doi:10.1038/srep00404.

Xie, P., J. E. Janowiak, P. A. Arkin, and R. Adler, 2003: GPCP pentad precipitation analyses: An experimental dataset based on gauge observations and satellite estimates. *J. Climate*, **16**, 2197–2214, doi:10.1175/2769.1.

Xu, X., and Coauthors, 2002: A comprehensive physical pattern of land-air dynamic and thermal structure on the Qinghai-Xizang Plateau. *Sci. China*, **45D**, 577–594, doi:10.1360/02yd9060.

Yanai, M., and C. Li, 1994: Mechanism of heating and the boundary layer over the Tibetan Plateau. *Mon. Wea. Rev.*, **122**, 305–323, doi:10.1175/1520-0493(1994)122<0305:MOHATB>2.0.CO;2.

——, ——, and Z. Song, 1992: Seasonal heating of the Tibetan Plateau and its effects on the evolution of the Asian summer monsoon. *J. Meteor. Soc. Japan*, **70**, 319–351.

Yang, K., T. Koike, and D. Yang, 2003: Surface flux parameterization in the Tibetan Plateau. *Bound.-Layer Meteor.*, **106**, 245–262, doi:10.1023/A:1021152407334.

——, ——, H. Fujii, T. Tamura, X. Xu, L. Bian, and M. Zhou, 2004: The daytime evolution of the atmospheric boundary layer and convection over the Tibetan Plateau: Observations and simulations. *J. Meteor. Soc. Japan*, **82**, 1777–1792, doi:10.2151/jmsj.82.1777.

Zhang, G., X. Xu, and J. Wang, 2003: A dynamic study of Ekman characteristics by using 1998 SCSMEX and TIPEX boundary layer data. *Adv. Atmos. Sci.*, **20**, 349–356, doi:10.1007/BF02690793.

Zhang, Q., J. Zhang, J. Qiao, and S. Wang, 2011: Relationship of atmospheric boundary layer depth with thermodynamic processes at the land surface in arid regions of China. *Sci. China*, **54D**, 1586–1594, doi:10.1007/s11430-011-4207-0.

——, H. Li, and J. Zhao, 2012: Modification of the land surface energy balance relationship by introducing vertical sensible heat advection and soil heat storage over the Loess Plateau. *Sci. China*, **55D**, 580–589, doi:10.1007/s11430-011-4220-3.

Zuo, H., Y. Hu, D. Li, S. Lu, and Y. Ma, 2005: Seasonal transition and its boundary layer characteristics in Anduo area of Tibetan Plateau. *Prog. Nat. Sci.*, **15**, 239–245, doi:10.1080/10020070512331342050.